Journal of Materials Chemistry

Dynamic Article Links

Cite this: J. Mater. Chem., 2012, 22, 23395

www.rsc.org/materials

PAPER

UV-visible-light-activated photocatalysts based on $Bi_2O_3/Bi_4Ti_3O_{12}/TiO_2$ double-heterostructured TiO_2 nanobelts†

Zhenhuan Zhao,[a] Jian Tian,[a] Dongzhou Wang,[a] Xueliang Kang,[a] Yuanhua Sang,[a] Hong Liu,*[ac] Jiyang Wang,[a] Shaowei Chen,*[b] Robert I. Boughton[d] and Huaidong Jiang[a]

Received 13th July 2012, Accepted 17th September 2012
DOI: 10.1039/c2jm34580c

Surface engineering of TiO_2 nanobelts by the controlled assembly of functional heterostructures represents an effective approach for the synthesis of high-performance photocatalysts. In this study, we prepared a novel $Bi_2O_3/Bi_4Ti_3O_{12}/TiO_2$ double-heterostructured nanobelt by depositing bismuth hydroxide onto the TiO_2 nanobelt surface. A thermal annealing treatment led to the formation of a $Bi_4Ti_3O_{12}$ interlayer that functioned as a bridge to link Bi_2O_3 and TiO_2. The double-heterostructured TiO_2 nanobelts exhibited better UV light photocatalytic performance than commercial P25. Importantly, the photocatalytic activity in the visible range was markedly better than that of Bi_2O_3 and Bi_2O_3/TiO_2 heterostructured TiO_2 nanobelts. The enhanced performance was accounted for by the material band structures where the matching was improved by the unique interlayer.

Introduction

Since Fujishima and Honda demonstrated the possibility of water splitting on an illuminated TiO_2 electrode surface in 1972,[1] the photocatalytic properties of metal–oxide semiconductors have been thoroughly investigated, in particular, in semiconductor modification and sensitization.[2,3] Among this, photocatalytic degradation of toxic organic pollutants in air and water by using TiO_2-based photocatalysts has represented an important area of research, primarily because of the materials' chemical inertness, non-photocorrosion, low cost, and non-toxicity.[4–11] However, because of the large intrinsic materials band gap, TiO_2 lacks sensitivity to visible light, and the practical applications of the TiO_2-based materials are still quite limited with the high recombination rate of the photogenerated electron–hole pairs under UV light irradiation.[12]

Much effort has been devoted to improving the photocatalytic performance of TiO_2. For example, the performance of TiO_2 can be enhanced by, for instance, coupling with a narrow band gap semiconductor, doping with metal or nonmetal ions,[13–15] sensitization with organic polymers,[16,17] and deposition of noble metals. It has been found that these strategies lead to not only improved separation of electron–hole pairs, but also manipulation of the band structure. For instance, Zyoud *et al.* reported that the core–shell structure of TiO_2/CdS efficiently degraded phenazopyridine under visible light illumination, and yet decomposed and leached out hazardous Cd^{2+} ions into water.[18] In another study, Bi_2S_3/TiO_2 and CdS/TiO_2 heterostructures were found to absorb visible light, and exhibited apparent photocatalytic activity in the degradation of Orange II.[19] Ion-doped anatase TiO_2 also exhibits absorption in the visible region. It is proposed that Fe^{3+} is not only an effective electron trap, but can also serve as a hole trap because the energy level of Fe^{3+}/Fe^{4+} lies above the valence band edge of anatase TiO_2.[20] Photodeposition of Ag or Au nanoparticles on TiO_2 also leads to the generation of photoactive sites that can efficiently improve the separation of photogenerated electron–hole pairs.[21,22]

In these studies, TiO_2 of different structures has been developed, such as nanowires,[23] nanorods,[24–27] nanotubes,[25,28] and nanobelts.[29–31] Further exotic surface geometries can be prepared by surface modification to form heterostructures. For instance, functional materials such as CdS,[32,33] PbS,[34] CdTe,[35] Bi_2WO_6,[36] Ag_2O,[37] and NiO,[38] have been used to prepare heterostructures in conjunction with one-dimensional TiO_2. Our group has exerted much effort to assemble heterostructures on TiO_2 nanobelts in order to improve the UV-visible photocatalytic performance. However, the mismatch between some visible photocatalysts and TiO_2 is a great obstacle in obtaining high performance UV-visible photocatalysts. Recently, a double nanoheterostructure based on Ag/TiO_2 nanoparticles/TiO_2 nanobelts was prepared by an acid-assisted hydrothermal method followed by an *in situ* photoreduction process. It was found that the double nanoheterostructure can further enhance the photocatalytic properties of the TiO_2 nanobelts in a dramatic fashion.[39] This result

[a]*State Key Laboratory of Crystal Materials, Center of Bio & Micro/nano Functional Materials, Shandong University, 27 Shandanan Road, Jinan 250100, China. E-mail: hongliu@sdu.edu.cn; shaowei@ucsc.edu*
[b]*Department of Chemistry and Biochemistry, University of California, 1156 High Street, Santa Cruz, California 95064, USA*
[c]*Beijing Institute of Nanoenergy and Nanosystems, Chinese Academy of Science, Beijing 100864, China*
[d]*Department of Physics and Astronomy, Bowling Green State University, Bowling Green, OH 43403, USA*
† Electronic supplementary information (ESI) available. See DOI: 10.1039/c2jm34580c

provides a clue that the band structures can be adjusted by the interphase between the visible photolysis component and the TiO_2 nanobelt. We suggest that the interphase may play an important role in separating the electron–hole pair. It should be pointed out that the preparation of the above double heterostructure is factually uncontrollable.

Therefore, constructing a double-heterostructured TiO_2 nanobelt under controllable conditions will be the most efficient methodology. Bi_2O_3 is an important semiconductor with a band gap of 2.8 eV that is narrower than that of TiO_2 (3.2 eV).[40] In fact, Bi_2O_3 has been used as an effective photocatalyst under visible light illumination, and coupling Bi_2O_3 with other photocatalysts exhibits enhanced photocatalytic efficiency in the decomposition of organic pollutants in water.[41–43] $Bi_4Ti_3O_{12}$ has also been found to possess photocatalytic activity in the degradation of organic pollutants in water under visible light illumination.[44,45] In this study, by using a simple annealing procedure, a new $Bi_2O_3/Bi_4Ti_3O_{12}/TiO_2$ double-heterostructured nanobelt was synthesized with the $Bi_4Ti_3O_{12}$ phase functioning as a bridge to link Bi_2O_3 and TiO_2. The heterostructure was confirmed by SEM, XRD, and HRTEM measurements, and the photocatalytic activity was highlighted by the photodegradation of methyl orange (MO) under UV light and visible light irradiations.

Experimental section

Materials

Sodium hydroxide (NaOH, analytic grade), hydrochloric acid (HCl), sulfuric acid (H_2SO_4), bismuth nitrate ($Bi(NO_3)_3 \cdot 5H_2O$), and nitric acid (HNO_3) were used directly without further purification. Deionized water was used throughout the experiments. Titania P25 (TiO_2, *ca.* 80% anatase and 20% rutile) was used as the Ti precursor to prepare TiO_2 nanobelts.

Preparation of TiO_2 nanobelts

An alkali hydrothermal process was employed for the preparation. In a typical procedure, 0.30 g of commercial TiO_2 powder (P25) was dispersed in 60 mL of a 10 M NaOH aqueous solution and placed into a 80 mL Teflon-lined autoclave. The autoclave was heated to and maintained at 200 °C for 72 h. The precipitate was collected and washed thoroughly with deionized water, followed by filtration and then immersion in 0.1 M HCl aqueous solution for 48 h. The resulting samples were hydrogen titanate nanobelts. These nanobelts were then added into a Teflon-lined autoclave containing 60 mL of a 0.02 M H_2SO_4 aqueous solution and maintained at 100 °C for 12 h. The products were collected after filtration, washing and air-drying. After thermal annealing at 600 °C for 2 h, TiO_2 nanobelts with a roughened surface were obtained.

Preparation of double-heterostructured photocatalysts

$Bi_2O_3/Bi_4Ti_3O_{12}/TiO_2$ photocatalysts were prepared by a chemical liquid co-precipitation method combined with an annealing process. In brief, 0.097 g of $Bi(NO_3)_3 \cdot 5H_2O$ was added to 10 mL of a 1.0 M nitric acid solution, followed by ultrasonification for 30 min to obtain a transparent solution. 0.08 g of TiO_2 nanobelts was added to the above solution. The mixture was sonicated for 10 min and gently stirred for another 30 min. Then 100 mL of a 0.2 M sodium hydroxide solution was dropped into the mixture over a period of 3 h. The white precipitate was collected by filtration, and washed with deionized water followed by drying at 70 °C. Finally, the catalysts were obtained by annealing the precipitate at 500 °C for 1 h. Pure Bi_2O_3 was also prepared *via* a similar procedure without the addition of TiO_2 nanobelts.

$Bi_4Ti_3O_{12}$ was prepared by the following procedure. First, 0.97 g $Bi(NO_3)_3 \cdot 5H_2O$ was dispersed in a 10 mL nitric acid solution at a concentration of 1.0 M to obtain a clear solution. Then 0.0015 mol P25 powder was added to the above solution. After sonication for 10 min, 100 mL of a sodium hydroxide solution (0.2 M) was slowly dropped into the above mixture. Then the precipitate was collected and washed with deionized water, followed by filtration and drying. Finally, $Bi_4Ti_3O_{12}$ was obtained by annealing the product at 600 °C for 1 h.

Characterization

The X-ray powder diffraction (XRD) patterns of the catalysts were recorded with a Bruker D8 Advance powder X-ray diffractionmeter with Cu Kα radiation ($\lambda = 0.15406$ nm) over a 2θ scan range between 20° and 80°. A HITACHI S-4800 field-emission scanning electron microscope (FE-SEM) was used to characterize the morphology and size of the synthesized catalysts. High-resolution transmission electron microscope (HRTEM) images were obtained with a JEOL JEM 2100F microscope. The UV-vis diffuse reflectance spectra (DRS) of the catalysts were acquired with a UV-vis spectrophotometer (UV 2550, Shimadzu) with an integrating sphere attachment. $BaSO_4$ was used as the reflectance standard, and the analytical range was 200 to 600 nm. Photoluminescence spectra (PL) were recorded by using a FLS920 fluorescence spectrometer with an excitation wavelength of 380 nm. The specific surface area was calculated using the Brunauer–Emmett–Teller (BET) method using the measurement instrument (Micromeritics, ASAP2020). The infrared spectrum was recorded on a Nexus 670 FT-IR spectrometer.

Photocatalytic assessments

Methyl orange (MO), a well-known acid–base indicator, was used as the model pollutant. In a typical experiment, 20 mL of an MO aqueous solution at a concentration of 20 mg L^{-1} and 20 mg of the as-synthesized catalyst powder were placed in a quartz reactor. Before illumination, the suspension was magnetically stirred in the dark for 30 min to establish an adsorption/desorption equilibrium between MO and the surface of the photocatalysts. The photocatalytic reaction was carried out at room temperature. A 300 W mercury lamp with a primary wavelength of 365 nm, and a 350 W Xe arc lamp were used as the UV and visible light source, respectively. At fixed illumination time intervals, the mixture was centrifuged to remove the catalyst particles for analysis. The concentration of MO was analyzed with a UV-vis spectrophotometer (UV-2102PC) by monitoring the absorbance at 465 nm. In a similar fashion, the photocatalytic activities of Bi_2O_3, $Bi_4Ti_3O_{12}$ and P25 powder were also investigated and compared.

 This journal is © The Royal Society of Chemistry 2012

Results and discussion

Fig. 1 depicts the XRD patterns of the TiO_2 nanobelts, Bi_2O_3, $Bi_4Ti_3O_{12}$ nanoparticles and $Bi_2O_3/Bi_4Ti_3O_{12}/TiO_2$ double-heterostructured nanobelts prepared at 500 °C with a 1 : 2 Bi_2O_3/TiO_2 weight ratio. The diffraction peaks of the TiO_2 nanobelts can be indexed to anatase TiO_2 with characteristic diffraction peaks (2θ) at 25.3°, 37.7°, 47.8°, 53.8°, 55°, 62.6°, 70.2° and 75.2° (JCPDS card 21-1272) (Fig. 1a). The high intensity and sharpness of the diffraction peaks of the Bi_2O_3 sample indicate a high degree of crystallinity of the sample and all the peaks can be assigned to monoclinic bismite according to JCPDS card no. 65-2366 (Fig. 2b). The XRD patterns of $Bi_4Ti_3O_{12}$, as shown in Fig. 1c, indicate that the prepared sample exhibits a well-crystallized perovskite phase corresponding to JCPDS card no. 35-0795. As shown in Fig. 1d, the main peaks of the double-heterostructured nanobelts (at 2θ = 25.2°, 27.4° and 30.01°) show that Bi_2O_3 and $Bi_4Ti_3O_{12}$ coexist on the surface of the TiO_2 nanobelts.

To investigate the crystalline phase of the Bi_2O_3–TiO_2 nanobelt composite system, TiO_2 nanobelts modified with bismuth hydroxide at the same Bi_2O_3/TiO_2 weight ratio of 6 : 1 were calcined at different temperatures. Fig. 2 shows the XRD patterns of the heterostructured Bi_2O_3–TiO_2 composites prepared at 300 °C, 500 °C, and 600 °C, with the corresponding camera pictures included in Fig. S1.† It can be seen from Fig. 2a that when bismuth hydroxide was deposited onto TiO_2 nanobelts and annealed at 300 °C, no obvious peaks emerged in the diffraction pattern of the products except a relatively broad peak located at 2θ = 27.4°. This peak can be assigned to the (120) plane of monoclinic Bi_2O_3 (according to JCPDF card no. 65-2366, shown in Fig. 2d). This suggests that at this temperature the TiO_2 nanobelts were modified with monoclinic Bi_2O_3. When the annealing temperature was raised to 500 °C, in addition to the peak at 27.4°, two sharp peaks at 2θ = 30.01° and 32.7° also appeared in the diffraction patterns (Fig. 2b). These can be indexed to the (171) and (200) planes of orthorhombic $Bi_4Ti_3O_{12}$ (according to JCPDF card no. 35-0795, shown in Fig. 2e). Note that this temperature at which the $Bi_4Ti_3O_{12}$ layer began to form is different from that reported by Yao *et al.* where the diffraction peak for the (171) planes started to emerge at an annealing temperature of 400 °C.[45] The appearance of both $Bi_4Ti_3O_{12}$ and Bi_2O_3 phases indicates that indeed $Bi_2O_3/Bi_4Ti_3O_{12}/TiO_2$ double-heterostructured nanobelts were prepared at this temperature. With a further increase of the annealing temperature to 600 °C, as shown in Fig. 2c, the diffraction peak of the (120) plane disappears and only those of $Bi_4Ti_3O_{12}$ remained, according to JCPDF card no. 35-0795 (Fig. 2e), suggesting that only $Bi_4Ti_3O_{12}/TiO_2$ heterostructured nanobelts were formed instead.

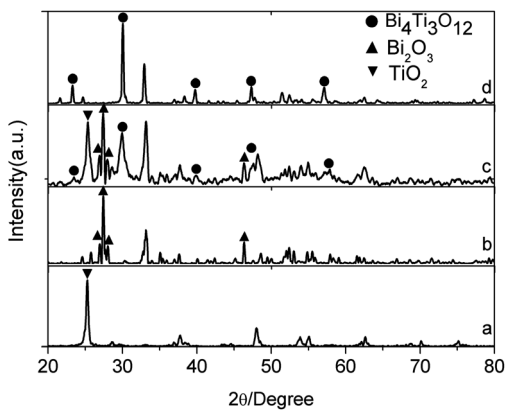

Fig. 1 XRD patterns of (a) TiO_2 nanobelts, (b) Bi_2O_3 powder, (c) $Bi_2O_3/Bi_4Ti_3O_{12}/TiO_2$ heterostructured nanobelts annealed at 500 °C with 1 : 2 Bi_2O_3/TiO_2 weight ratio, and (d) $Bi_4Ti_3O_{12}$ particles.

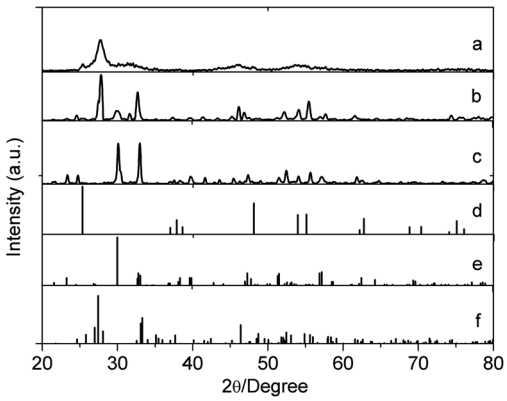

Fig. 2 XRD patterns of products prepared by annealing TiO_2 nanobelts deposited with bismuth hydroxide at 300 °C (a), 500 °C (b) and 600 °C (c). Bi_2O_3/TiO_2 weight ratio is 6 : 1. (d)–(f) refer to JCPDS card no. 21-1272 for TiO_2, 35-0795 for $Bi_4Ti_3O_{12}$ and 65-2366 for Bi_2O_3, respectively.

The emergence of $Bi_4Ti_3O_{12}$ at an annealing temperature of 500 °C is most likely the result of the reactions between Bi_2O_3 and TiO_2 particles. According to Zhou *et al.*, when TiO_2 nanobelts were treated with acid, anatase TiO_2 nanoparticles were recrystallized on the surface of the TiO_2 nanobelts,[39] while Bi_2O_3 particles were formed due to the dehydration of bismuth hydroxide. The etching of TiO_2 nanobelts can be divided into two processes performed at the same time. The first one is the formation of TiO_2 nanoparticles on the surface of $H_2Ti_3O_7$ nanobelts. In H_2SO_4 solution, the $H_2Ti_3O_7$ nanobelts react with hydrogen ions to obtain Ti^{4+} ions which hydrolyzed to form TiO_2 nanoparticles through heterogeneous nucleation. The second one is the formation of the large number of pits on the surface of the $H_2Ti_3O_7$ nanobelts. The pits link together to form island-like $H_2Ti_3O_7$ nanoparticles on the surface of the $H_2Ti_3O_7$ nanobelts. The $H_2Ti_3O_7$ nanobelts and $H_2Ti_3O_7$ island-like nanoparticles can be transferred into TiO_2 by calcining at 600 °C. In addition, it should be noticed that no obvious anatase TiO_2 diffraction peak can be observed in the diffraction patterns of the products prepared at the controlled temperatures. This is due to the large difference of the thermal expansion coefficient between Bi_2O_3 ($\alpha = 15 \times 10^{-6}$ K^{-1})[46] and anatase TiO_2 ($\alpha = 8.6 \times 10^{-6}$ K^{-1}).[47] Initially only amorphous $Bi(OH)_3$ particles were precipitated onto the nanobelt surface. At elevated temperatures, $Bi(OH)_3$ underwent dehydration and formed Bi_2O_3 nanoparticles that were closely attached to the TiO_2 nanobelt surface. When the composite nanobelts cooled down, the shrinkage of the Bi_2O_3 nanoparticle was much greater than that of the nanobelts. Therefore, a strong compressive stress was applied to the nanobelt, leading to distortion of the crystalline lattice, and hence broadening and even disappearance of the XRD diffraction peaks.

The morphologies of the as-synthesized TiO_2 nanobelts, acid treated TiO_2 nanobelts, Bi_2O_3 powders, $Bi_4Ti_3O_{12}$ particles and $Bi_2O_3/Bi_4Ti_3O_{12}/TiO_2$ double-heterostructured nanobelts were then examined using a field-emission scanning electron microscope (FESEM). As displayed in Fig. 3(a), the TiO_2 nanobelt exhibits a width of 40 to 150 nm, and length up to dozens of micrometers. The inset in Fig. 3(a) shows the end of a nanobelt, where a smooth surface and rectangular cross-section can be identified. After an acid treatment, the surface of the TiO_2 nanobelts became roughened and decorated with numerous TiO_2 particles and pits, which were thought to be the origin of the large specific surface area and large quantity of active facets, as shown in Fig. 3(b). The SEM images of the as-synthesized Bi_2O_3 powders and $Bi_4Ti_3O_{12}$ particles are shown in Fig. 3(c) and (d), with the dimensions in the range of a few microns and a few hundred nm, respectively. Fig. 3(e) is the SEM image of the $Bi_2O_3/Bi_4Ti_3O_{12}/TiO_2$ double-heterostructured nanobelts prepared at 500 °C with a 6 : 1 Bi_2O_3/TiO_2 weight ratio. One can see that the composites still maintain the belt shape with numerous secondary particles deposited on the surface. The mean size of the secondary particles is about 25 nm. Notably, the secondary particles are uniformly distributed over the belts without apparent aggregation. This large surface area is beneficial to the growth and uniform distribution of secondary nanostructures. A typical TEM image of an individual heterostructural nanobelt is shown in Fig. 3(f). As can be seen, the secondary nanoparticles display an average size of 25 nm, which is consistent with the results from FESEM analysis.

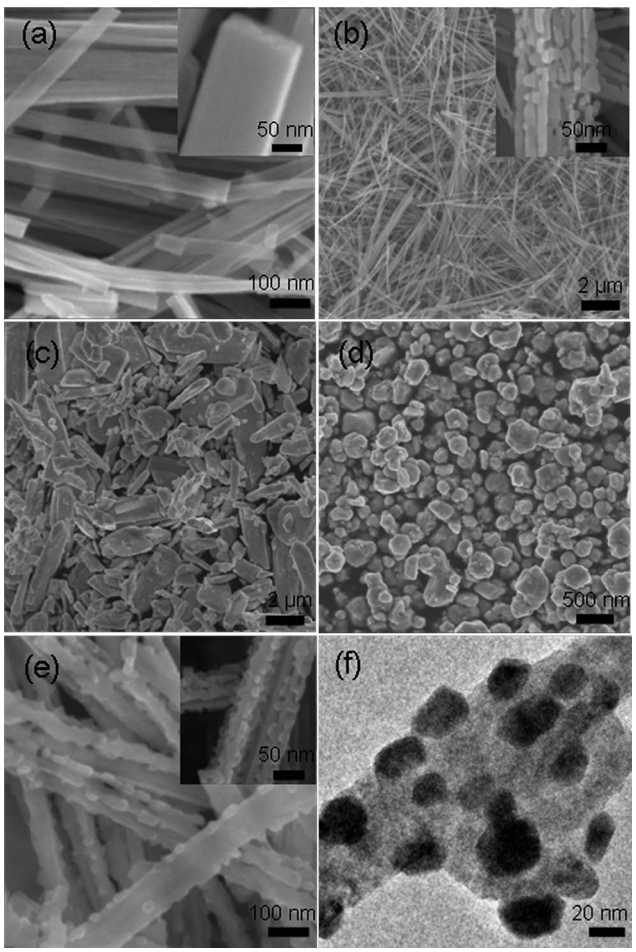

Fig. 3 Typical SEM images of (a) TiO_2 nanobelts, (b) TiO_2 nanobelts treated with acid, (c) Bi_2O_3 powder, (d) $Bi_4Ti_3O_{12}$ particles, (e) $Bi_2O_3/Bi_4Ti_3O_{12}/TiO_2$ double-heterostructured nanobelts with a Bi_2O_3/TiO_2 weight ratio of 6 : 1 prepared at 500 °C and (f) corresponding TEM images of the heterostructure.

The structure of the double-heterostructured TiO_2 nanobelts was further studied by high-resolution TEM measurements, as shown in Fig. 4. Fig. 4(b)–(d) show the Fast-Fourier-transform (FFT) patterns of the selected areas in panel (a). In panel (a), the large substrate area can be identified as anatase TiO_2 with a growth direction of [010] (ref. 29) (Fig. S2†). As shown in Fig. S2,† the prepared TiO_2 nanobelts are single crystalline, and belong to the tetragonal phase. The lattice fringes perpendicular to the growth direction are determined to be 0.35 nm, consistent with the lattice parameter according to JCPDF card no. 21-1272. The nanoparticle crystalline lattice is conjoined with the TiO_2 lattice to form a heterostructure. Importantly, one can see that the interfacial region exhibited markedly different fringes in comparison with TiO_2 or Bi_2O_3 (panel a), and the corresponding FFT patterns (panel c) showed a rectangular symmetry that corresponds to the electron diffraction of an orthorhombic $Bi_4Ti_3O_{12}$ crystal. This is markedly different from those of Bi_2O_3 as shown in panels (b) and (d), where the FFT patterns showed a diamond symmetry with an included angle of 73.9°, corresponding to the electron diffraction patterns of monoclinic Bi_2O_3. Note that the included angle is larger than the theoretical value, 67.7° (JCPDF card no. 65-2366), which is probably caused by the stress originating from the mismatch of lattice parameters and thermal expansion between $Bi_4Ti_3O_{12}$ and Bi_2O_3. The thermal expansion coefficient of $Bi_4Ti_3O_{12}$ is 11.5×10^{-6} K^{-1},[48] which is in the intermediate range between Bi_2O_3 ($\alpha = 15 \times 10^{-6}$ K^{-1})[46] and anatase TiO_2 ($\alpha = 8.6 \times 10^{-6}$ K^{-1}).[47] Nevertheless, both the XRD and HRTEM results confirm the existence of $Bi_2O_3/Bi_4Ti_3O_{12}/TiO_2$ double-heterostructures on the TiO_2 nanobelt surface, which extended the optical absorption of nanobelts to the visible range, as detailed below.

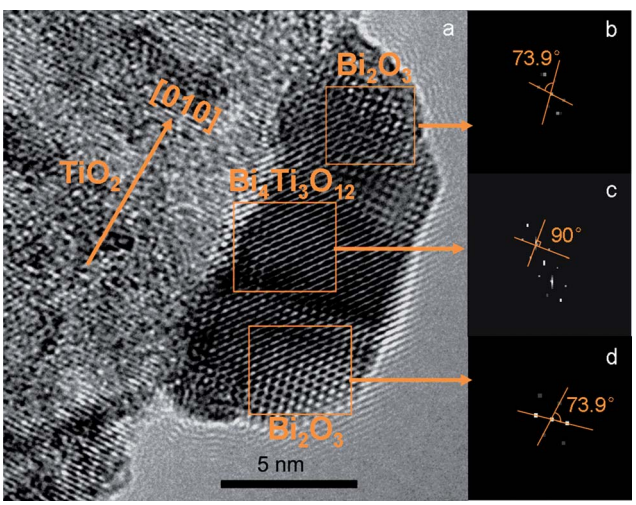

Fig. 4 HRTEM of a double-heterostructured TiO_2 nanobelt obtained at 500 °C with a Bi_2O_3/TiO_2 weight ratio of 6 : 1 (a). (b)–(d) show Fourier transform patterns of selected areas.

This journal is © The Royal Society of Chemistry 2012

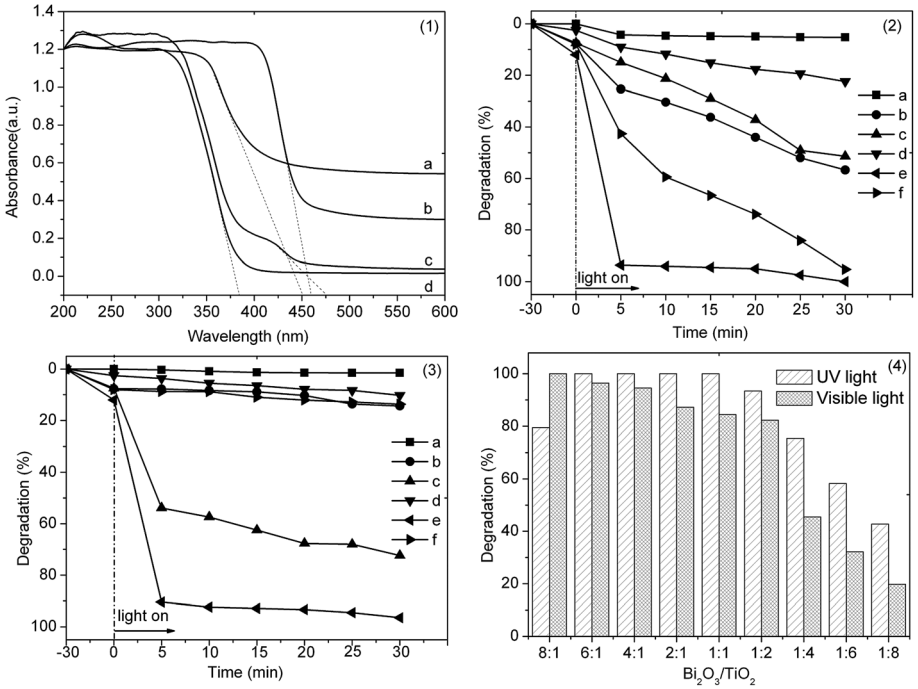

Fig. 5 (1) UV-vis DRS of (a) $Bi_4Ti_3O_{12}$ particles, (b) Bi_2O_3 powder, (c) $Bi_2O_3/Bi_4Ti_3O_{12}/TiO_2$ double-heterostructured nanobelts with a Bi_2O_3/TiO_2 weight ratio of 1 : 2 prepared at 500 °C and (d) TiO_2 nanobelts; (2) and (3) photocatalytic degradation of MeO under UV light and visible light irradiation, respectively, without the addition of any catalyst (a), and degradation in the presence of (b) TiO_2 nanobelts treated with acid corrosion, (c) Bi_2O_3 powder, (d) $Bi_4Ti_3O_{12}$ particles, (e) the $Bi_2O_3/Bi_4Ti_3O_{12}/TiO_2$ heterostructure obtained at 500 °C with 6 : 1 Bi_2O_3/TiO_2 weight ratio and (f) P25; (4) photocatalytic degradation of MeO under UV and visible light irradiation for 30 min in the presence of the $Bi_2O_3/Bi_4Ti_3O_{12}/TiO_2$ double heterostructure obtained at 500 °C.

Fig. 5(1) shows the UV-vis absorption spectra of TiO_2 nanobelts, Bi_2O_3 powder, $Bi_4Ti_3O_{12}$ particles and $Bi_2O_3/Bi_4Ti_3O_{12}/TiO_2$ double-heterostructured nanobelts. Both $Bi_4Ti_3O_{12}$ and Bi_2O_3 show significant absorption up to the visible range of 600 nm (curve a and b). TiO_2 nanobelts exhibit only apparent absorption in the UV region (<380 nm, curve d). Interestingly, the double-heterostructure shows greatly enhanced absorption in the visible region as well (curve c). The absorption edge of TiO_2 nanobelts, Bi_2O_3 particles, $Bi_4Ti_3O_{12}$ nanoparticles and $Bi_2O_3/Bi_4Ti_3O_{12}/TiO_2$ double-heterostructured nanobelts is determined to be 380 nm, 460 nm, 450 nm and 475 nm, respectively, according to Fig. 5(1). Therefore, their respective band gap energy is evaluated to be 3.2 eV, 2.69 eV, 2.76 eV and 2.61 eV.

In order to evaluate the photocatalytic properties of the prepared catalysts, MO was chosen as a model organic pollutant. To eliminate the effect of MO absorption on the photocatalytic activity, the photocatalyst suspension was placed in the dark for 30 min to reach an adsorption–desorption equilibrium of MO on the catalysts. The difference between the initial absorption intensity at a certain reaction time and the residual intensity of the MO solution ($C_0 - C_t$) divided by the initial absorption intensity (C_0) represents the degree of degradation. Fig. 5(2) shows the photocatalytic degradation of MO in water as a function of time under UV irradiation in the absence and presence of varied catalysts. Without the aid of any catalysts, MO cannot be decomposed by itself. $Bi_2O_3/Bi_4Ti_3O_{12}/TiO_2$ nanobelts display dramatic improvement in the photocatalytic activity with about 95% of MO decomposed after five min and 100% after 30 min of UV light illumination (curve e). This efficiency is remarkable even when compared with that of P25 which also decomposed about 100% of MO within 30 min of UV illumination but the reaction rate was much lower. Overall, the results demonstrated that TiO_2 nanobelts functionalized with double heterostructures of $Bi_2O_3/Bi_4Ti_3O_{12}$ exhibited the best photocatalytic activity in MO degradation under UV irradiation. This may be ascribed to the reduced recombination dynamics of photogenerated electron–hole pairs (more details below).

The photocatalytic activities of the varied catalysts in the visible range were also evaluated and compared. A 350 W Xenon lamp was now used as the visible light source with filters to eliminate UV light. The photodegradation curves of MO in water as a function of irradiation time in the absence and presence of varied catalysts are depicted in Fig. 5(3). Again, no degradation of MO was observed in the absence of a catalyst (curve a). For acid-treated TiO_2 nanobelts (curve b), $Bi_4Ti_3O_{12}$ particles (curve d), and P25 (curve f) the photocatalytic activity was very low with only *ca.* 10% of MO decomposed after 30 min of visible light illumination. In contrast, Bi_2O_3 powders displayed very apparent photocatalytic activity with 75% of MO decomposed after 30 min of light illumination (curve c). More interestingly, the $Bi_2O_3/Bi_4Ti_3O_{12}/TiO_2$ double-heterostructured nanobelts display an even higher visible light photocatalytic activity in the degradation of MO (curve e), again, with close to 90% of MO decomposed after 5 min and close to 100% after 30 min of visible light irradiation.

We also examined the impacts of the Bi_2O_3/TiO_2 weight ratio on the photocatalytic activity of the double-heterostructured nanobelts. As shown in Fig. 5(4), under visible light irradiation, the fraction of MO decomposed after 30 min of illumination decreases monotonically with decreasing Bi_2O_3/TiO_2 weight ratio, with a somewhat small variation from ~100% at 8 : 1 to ~90% at 1 : 2, and then a much more rapid diminishment to less than 20% at 1 : 8. This may be due to the decrease of the amount of Bi_2O_3 loaded onto the surface of the TiO_2 nanobelts that reduced the absorption of visible photons. A somewhat different behavior was observed with UV light irradiation. At the weight ratio of 8 : 1 the degradation of MO after 30 min of illumination was only 80%. It increases markedly to almost 100% when the weight ratio increases to between 6 : 1 and 1 : 1. At higher weight ratio, the degradation efficiency exhibited an apparent diminishment, with 90% of MO decomposed at 1 : 2 to less than 40% at 1 : 8.

As stated previously, the $Bi_2O_3/Bi_4Ti_3O_{12}/TiO_2$ double-heterostructured nanobelts were prepared at 500 °C. The Bi_2O_3/TiO_2 heterostructure and the $Bi_4Ti_3O_{12}/TiO_2$ composite were obtained at 300 °C and 600 °C, respectively. In order to clarify the effect of annealing temperature on the photocatalytic activity, the photodegradation of MO was also analyzed by using the three kinds of catalysts under both UV and visible light irradiation as a function of time. The results are shown in Fig. 6(1) and (2), respectively. It can be seen that all heterostructured catalysts exhibited apparent photocatalytic activities. Among these, the $Bi_2O_3/Bi_4Ti_3O_{12}/TiO_2$ double-heterostructured nanobelts that were prepared at 500 °C exhibited the highest photocatalytic activity in the decomposition of MO under either UV or visible light illumination (curves b). For the catalysts prepared at 300 °C, *i.e.*, the Bi_2O_3/TiO_2 heterostructured nanobelts (curves a), the activities were lower but still somewhat better than those prepared at 600 °C, *i.e.*, the $Bi_4Ti_3O_{12}/TiO_2$ composite (curves c). These results suggest that the optimal annealing temperature should be around 500 °C.

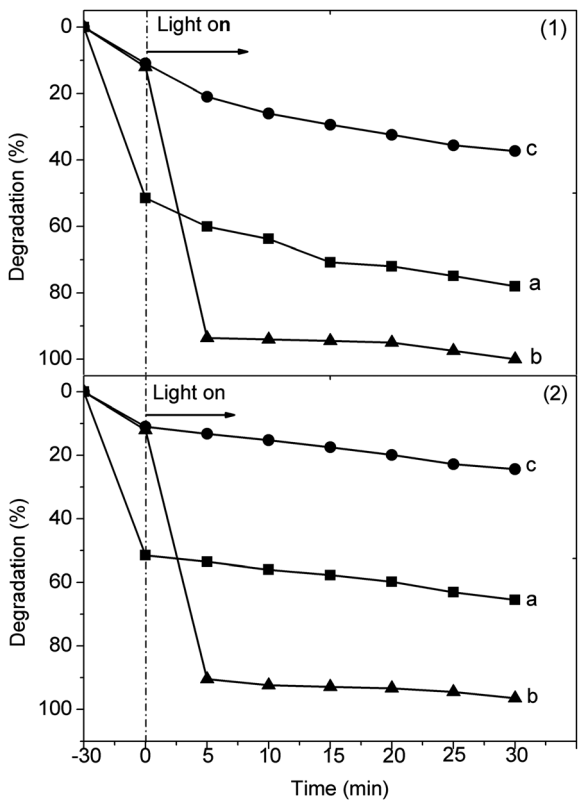

Fig. 6 Photocatalytic degradation of MeO under UV (1) and visible light (2) illumination with the heterostructure prepared at different temperatures with the same 6 : 1 Bi_2O_3/TiO_2 weight ratio. (a), (b) and (c) refer to 300 °C, 500 °C and 600 °C, respectively.

The excellent photocatalytic degradation of MO under UV and visible light irradiation should be due to the large specific area of the double-heterostructured $Bi_2O_3/Bi_4Ti_3O_{12}/TiO_2$ nanobelt. We evaluated the specific surface area of the prepared samples and the results are shown in Table 1 (see ESI†). As can be seen from Table 1,† the BET specific surface area of the pristine TiO_2 nanobelt is about 32.654 $m^2 g^{-1}$, while the specific surface area of the TiO_2 nanobelt treated with acid corrosion increases to 41.791 $m^2 g^{-1}$. The double-heterostructured $Bi_2O_3/Bi_4Ti_3O_{12}/TiO_2$ nanobelts prepared at 500 °C display a larger specific surface area (about 47.02 $m^2 g^{-1}$), which lead to the exposure of more active sites giving high photocatalytic activity. The specific surface area of the sample prepared at 300 °C and 600 °C is about 50.617 $m^2 g^{-1}$ and 27.589 $m^2 g^{-1}$, respectively. It should be noticed that the specific surface area increases with the increase of annealing temperature. The large specific area of the sample prepared at 300 °C should be due to the poor crystallinity (about 48%) which has a negative effect on the photocatalytic activity of the catalyst.

The stability of the double-heterostructured $Bi_2O_3/Bi_4Ti_3O_{12}/TiO_2$ nanobelt prepared at 500 °C under UV and visible light irradiation was also investigated. Fig. S3† shows the irradiation time dependence of photocatalytic degradation of MO in the presence of the double-heterostructured $Bi_2O_3/Bi_4Ti_3O_{12}/TiO_2$ nanobelt prepared at 500 °C repeated degradation experiments under UV and visible light irradiation. Unfortunately, the double-heterostructured nanobelt is unstable for repeated use both under UV and visible light irradiation. After being used four times, the color of the catalyst changed into dark green from original yellow (see Fig. S4†). The infrared spectrum of the double-heterostructured $Bi_2O_3/Bi_4Ti_3O_{12}/TiO_2$ nanobelt prepared at 500 °C was recorded and shown in Fig. S5.† It can be seen from Fig. S5† that the absorption bands of the sample before and after UV light irradiation show no changes, indicating that the variation of the color should not be induced by the adsorption of organic species. Therefore, we recorded the XRD patterns of the sample, shown in Fig. S6.† Fig. S6† shows the XRD patterns of (a) the double-heterostructured $Bi_2O_3/Bi_4Ti_3O_{12}/TiO_2$ nanobelts prepared at 500 °C, (b) the double heterostructure after being used four times under UV light irradiation, (c) the double heterostructure after being used four times under visible light irradiation, (d) and (e) refer to the double heterostructure annealed at 400 °C after repeated degradation experiments under UV and visible light irradiation, respectively. It can be seen from Fig. S6† that after repeated degradation experiments two new diffraction peaks (at $2\theta = 28.57$ and 29.2) can be found in the XRD patterns (curve b and c) and can be indexed to the (200) plane and (020) plane of monoclinic bismuth. Therefore, it is suggested that the formation of bismuth has a significantly negative effect on the photocatalytic activity of the heterostructure. The bismuth not only consumes the

 This journal is © The Royal Society of Chemistry 2012

photoinduced electrons, but also inhabits the harvesting of light. Fortunately, by annealing the dark green sample, the diffraction peaks of monoclinic bismuth disappear (curve d and e). The photocatalytic activity of the double heterostructure can be recovered, shown in Fig. S7.† We also immersed the dark green sample into hydrogen peroxide (30 wt%) and the photocatalytic degradation efficiency can also be recovered. (curve c and d in Fig. S7†).

In the above studies, the photocatalytic activity is closely related to the dynamics of the separation and recombination of photoinduced electrons and holes, which may impact the corresponding photoluminescence (PL) characteristics. From Fig. 7, it can be seen that at the excitation wavelength of 380 nm, acid-treated TiO_2 nanobelts displayed a strong and broad emission peak at about 460 nm (curve a), and the emission intensity significantly decreased with the loading of Bi_2O_3 onto the surface of the TiO_2 nanobelts (curve c). This may be because Bi_2O_3 and $Bi_4Ti_3O_{12}$ on TiO_2 nanobelts acted as traps for the photoinduced charge carriers.

The improved photocatalytic performance observed with the $Bi_2O_3/Bi_4Ti_3O_{12}/TiO_2$ double-heterostructured nanobelts might be explained by the band structure of the composite materials. Note that the conduction and valence band positions can be determined by using the following empirical equation,[49,50]

$$E_{CB} = X - E_e - 0.5\,E_g \quad (1)$$

where E_{CB} denotes the conduction band edge potential, X the geometric mean of the Mulliken electronegativity of the constituent atoms, E_e the energy of free electrons on the hydrogen scale (about 4.5 eV) and E_g the band gap. The X values for TiO_2, Bi_2O_3 and $Bi_4Ti_3O_{12}$ are about 5.81 eV, 6.23 eV and 4.12 eV, respectively,[40] and the corresponding E_g values are 3.2 eV, 2.69 eV, and 2.76 eV. Thus, the positions of the conduction band edge (E_{CB}) at the point of zero charge are estimated to be −0.29 eV, 0.38 eV, and −1.76 eV, respectively, as illustrated in Fig. 8.

Under UV illumination (Fig. 8(a)), for TiO_2 nanobelts alone, the valence band electrons were excited to produce electron–hole pairs which recombined rapidly. However, in the

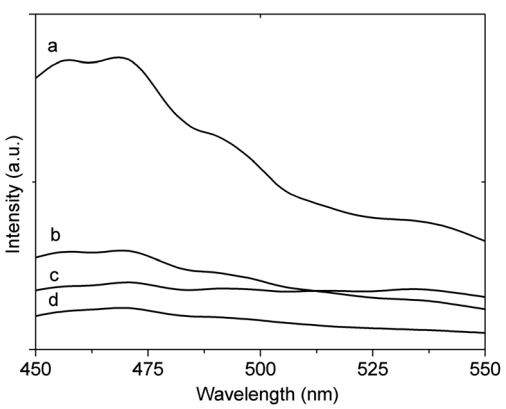

Fig. 7 Photoluminescence (PL) spectra of prepared products: (a) TiO_2 nanobelts, (b) $Bi_4Ti_3O_{12}$ particles, (c) $Bi_2O_3/Bi_4Ti_3O_{12}/TiO_2$ double-heterostructured nanobelts with 6 : 1 Bi_2O_3/TiO_2 weight ratio at 500 °C, and (d) Bi_2O_3 powder.

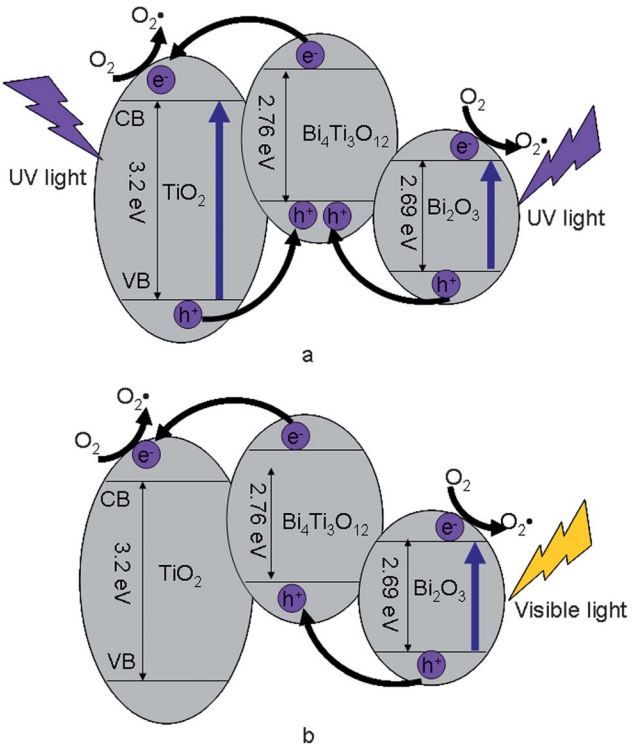

Fig. 8 Schematic diagrams for electron–hole pair separation under UV (a) and visible light (b) irradiation and the band structure in the $Bi_2O_3/Bi_4Ti_3O_{12}/TiO_2$ double heterostructure.

double heterostructures, electrons in both the valence band of TiO_2 and Bi_2O_3 can be excited. The photoinduced holes then flow into the valence band of the $Bi_4Ti_3O_{12}$ layer, while the electrons flow into the conduction bands of TiO_2 and Bi_2O_3. Meanwhile, the photogenerated electrons accumulate in the conduction band of Bi_2O_3 and react with adsorbed oxygen molecules to produce superoxide radical O_2^-, which generates the hydroperoxy $HO_2^{\cdot}$ radical through protonation and finally produces OH. Notably, it has been reported that $Bi_4Ti_3O_{12}$ with an orthorhombic symmetry consists of $(Bi_2O_2)^{2+}$ layers and $(Bi_2Ti_3O_{10})^{2-}$ units, and both of them can effectively separate the electron–hole pairs.[51] Holes in the valence band of Bi_2O_3 move into the valence band of $Bi_4Ti_3O_{12}$ and disturb the charge balance. Thus, electrons in the conduction band of $Bi_4Ti_3O_{12}$ migrate to the closest conduction band of TiO_2. With the accumulation of valence holes of Bi_2O_3 and TiO_2, free electrons are produced in the conduction band of $Bi_4Ti_3O_{12}$ (−1.76 eV) and they tend to migrate into the adjacent conduction band of TiO_2 (−0.29 eV) rather than the lower conduction band of Bi_2O_3 (0.38 eV). In addition, though the $Bi_4Ti_3O_{12}$ interlayer did not help increase the absorbance of light, it might play an important role in improving the separation of photoinduced electron–hole pairs from the $(Bi_2O_2)^{2+}$ layers and $(Bi_2Ti_3O_{10})^{2-}$ particles. Moreover, the resistance to electron and hole transport is very low due to the high crystallinity of the $Bi_4Ti_3O_{12}$ phase. Consequently, efficient electron–hole separation increases the lifetime of the charge carriers and enhances the photocatalytic activity of the $Bi_2O_3/Bi_4Ti_3O_{12}/TiO_2$ double-heterostructured nanobelts. The key steps of the photocatalytic reactions may be summarized below.

$$Bi_2O_3 + h\nu \rightarrow Bi_2O_3\,(h^+ + e^-) \quad (2)$$

$$Bi_2O_3\,(h^+) + Bi_4Ti_3O_{12} \rightarrow Bi_4Ti_3O_{12}\,(h^+) + Bi_2O_3 \quad (3)$$

$$Bi_2O_3\,(e^-) + O_2 \rightarrow O_2^- \quad (4)$$

$$TiO_2 + h\nu \rightarrow TiO_2\,(h^+ + e^-) \quad (5)$$

$$TiO_2\,(h^+) + Bi_4Ti_3O_{12} \rightarrow Bi_4Ti_3O_{12}\,(h^+) + TiO_2 \quad (6)$$

$$TiO_2\,(e^-) + O_2 \rightarrow O_2^- \quad (7)$$

$$O_2^- + H_2O \rightarrow OH_2^{\cdot} + OH^- \quad (8)$$

$$OH_2^{\cdot} + H_2O \rightarrow H_2O_2 + OH^{\cdot} \quad (9)$$

$$H_2O_2 \rightarrow 2OH^{\cdot} \quad (10)$$

Under visible light irradiation (Fig. 8(b)), the energy of a visible light photon (2.9 eV) is greater than the band gap energy of Bi_2O_3 (2.69 eV), but smaller than the band gap energy of TiO_2 (3.2 eV). Therefore, only electrons in the valence band of Bi_2O_3 can be excited to produce electrons and holes. The electrons then react with oxygen molecules and finally degrade MO in water under visible light irradiation. The enhancement of the visible light photocatalytic activity is most likely attributed to the double heterostructures and the $Bi_4Ti_3O_{12}$ interlayer for the highly efficient separation of charge carriers. It should be pointed out that there are still electrons that may migrate to the conduction band of TiO_2 and participate in photocatalytic reactions to decompose MeO.

Both Bi_2O_3 and $Bi_4Ti_3O_{12}$ are potential visible light catalysts in the decomposition of organic pollutants. Although the absorbance of visible light is related to Bi_2O_3, the role of $Bi_4Ti_3O_{12}$ should not be neglected. In fact, the double heterostructure exhibited much enhanced photocatalytic activity as compared to single heterostructures as the $Bi_4Ti_3O_{12}$ interlayer might efficiently improve the separation of photogenerated electron–hole pairs.

Conclusion

$Bi_2O_3/Bi_4Ti_3O_{12}/TiO_2$ double-heterostructured nanobelts were prepared by depositing bismuth hydroxide nanoparticles on the TiO_2 nanobelt surfaces, followed by an annealing procedure at 500 °C. The detailed morphology was characterized by FESEM and HRTEM measurements. The as-synthesized heterostructures displayed high photocatalytic activity under either UV or visible light illumination for the degradation of MO in water. The $Bi_4Ti_3O_{12}$ interlayer between TiO_2 and Bi_2O_3 was found to effectively separate photogenerated electron–hole pairs, as confirmed by the XRD, UV-vis DRS and PL spectroscopic measurements. Under UV light irradiation, both the conduction electrons of TiO_2 and Bi_2O_3 might be excited to improve the photocatalytic activity of the double heterostructures. Under visible light irradiation, Bi_2O_3 on the TiO_2 nanobelt surface acted as a visible light sensitizer and absorbed visible light photons to produce electron–hole pairs. The holes then flowed into the $Bi_4Ti_3O_{12}$ conduction band with an increasing charge carrier lifetime. It is proposed that excited electrons are responsible for the improvement of the photocatalytic performance of the $Bi_2O_3/Bi_4Ti_3O_{12}/TiO_2$ double-heterostructured nanobelts. $Bi_2O_3/Bi_4Ti_3O_{12}/TiO_2$ double-heterostructured TiO_2 nanobelts with high UV-vis photocatalysis property can be renewed by a simple heat-treatment or hydrogen peroxide.

Acknowledgements

This research was supported by National Natural Science Foundation of China (NSFDYS:5092505 and 51002089), Innovation Research Group (IRG: 51021062), The Natural Science Funds for Distinguished Young Scholar of Shandong Province (JQ201117) and the Independent Innovation Foundation of Shandong University (2010JQ004).

References

1 A. Fujishima and K. Honda, *Nature*, 1972, **238**, 37.
2 C. Z. Wenting Dong, *J. Phys. Chem. Solids*, 2003, **64**, 265.
3 D. R. Baker and P. V. Kamat, *Adv. Funct. Mater.*, 2009, **19**, 805.
4 F. Zhang, J. Zhao, T. Shen, H. Hidaka, E. Pelizzetti and N. Serpone, *Appl. Catal., B*, 1998, **15**, 147.
5 P. Qu, J. Zhao, T. Shen and H. Hidaka, *J. Mol. Catal. A: Chem.*, 1998, **129**, 257.
6 T. Wu, T. Lin, J. Zhao, H. Hidaka and N. Serpone, *Environ. Sci. Technol.*, 1999, **33**, 1379.
7 T. Minabe, D. A. Tryk, P. Sawunyama, Y. Kikuchi, K. Hashimoto and A. Fujishima, *J. Photochem. Photobiol., A*, 2000, **137**, 53.
8 Y. H. Hsien, C. F. Chang, Y. H. Chen and S. Cheng, *Appl. Catal., B*, 2001, **31**, 241.
9 F. B. Li and X. Z. Li, *Chemosphere*, 2002, **48**, 1103.
10 C. H. Ao and S. C. Lee, *Appl. Catal., B*, 2003, **44**, 191.
11 P. K. J. Robertson, L. A. Lawton, B. Münch and J. Rouzade, *Chem. Commun.*, 1997, 393.
12 G. Liu, L. Wang, H. G. Yang, H.-M. Cheng and G. Q. Lu, *J. Mater. Chem.*, 2010, **20**, 831.
13 J. Wang, D. N. Tafen, J. P. Lewis, Z. Hong, A. Manivannan, M. Zhi, M. Li and N. Wu, *J. Am. Chem. Soc.*, 2009, **131**, 12290.
14 G. Liu, L. Wang, C. Sun, X. Yan, X. Wang, Z. Chen, S. C. Smith, H.-M. Cheng and G. Q. Lu, *Chem. Mater.*, 2009, **21**, 1266.
15 X. Zong, C. Sun, Z. Chen, A. Mukherji, H. Wu, J. Zou, S. C. Smith, G. Q. Lu and L. Wang, *Chem. Commun.*, 2011, **47**, 6293.
16 D. Chowdhury, A. Paul and A. Chattopadhyay, *Langmuir*, 2005, **21**, 4123.
17 L. Gai, G. Du, Z. Zuo, Y. Wang, D. Liu and H. Liu, *J. Phys. Chem. C*, 2009, **113**, 7610.
18 A. H. Zyouda, N. Zaatara, I. Saadeddina, C. Alib, D. Parkc, G. Campetc and H. S. Hilala, *J. Hazard. Mater.*, 2010, **173**, 318.
19 Y. Bessekhouad, D. Robert and J. V. Weber, *J. Photochem. Photobiol., A*, 2004, **163**, 569.
20 J. Zhua, W. Zhenga, B. Hea, J. Zhanga and M. Anpo, *J. Mol. Catal. A: Chem.*, 2004, **216**, 35.
21 S. C. Chan and M. A. Barteau, *Langmuir*, 2005, **21**, 5588.
22 Y. Wang, G. Du, H. Liu, D. Liu, S. Qin, J. Wang, X. Tao, M. Jiang and Z. L. Wang, *J. Nanosci. Nanotechnol.*, 2009, **9**, 2119.
23 F. Xinjian, S. Karthik, O. K. Varghese, P. Maggie, T. J. Latempa and C. A. Grimes, *Nano Lett.*, 2008, **8**, 3781.
24 Y. Wang, L. Zhang, K. Deng, X. Chen and Z. Zou, *J. Phys. Chem. C*, 2007, **111**, 2709.
25 T. Akita, M. Okumura, K. Tanaka, K. Ohkuma, M. Kohyama, T. Koyanagi, M. Date, S. Tsubota and M. Haruta, *Surf. Interface Anal.*, 2005, **37**, 265.
26 S. J. Limmer and G. Cao, *Adv. Mater.*, 2003, **15**, 427.
27 X. Peng and A. Chen, *J. Mater. Chem.*, 2004, **14**, 2542.
28 L. K. Tan, X. Liuab and H. Gao, *J. Mater. Chem.*, 2011, **21**, 11084.
29 N. Wu, W. Jin, T. D. Nyago, W. Hong, Z. Jianguo, J. P. Lewis, L. Xiaogang, S. S. Leonard and M. Ayyakkannu, *J. Am. Chem. Soc.*, 2010, **132**, 6679.
30 W. Zhou, X. Liu, J. Cui, D. Liu, J. Li, H. Jiang, J. Wang and H. Liu, *CrystEngComm*, 2011, **13**, 4557.

 This journal is © The Royal Society of Chemistry 2012

31 W. Zhou, H. Liu, R. I. Boughton, G. Du, J. Lin, J. Wang and D. Liu, *J. Mater. Chem.*, 2010, **20**, 5993.
32 H. Jia, H. Xu, Y. Hu, Y. Tang and L. Zhang, *Electrochem. Commun.*, 2007, **9**, 354.
33 J. Cao, J.-Z. Sun, H.-Y. Li, J. Hong and M. Wang, *J. Mater. Chem.*, 2004, **14**, 1203.
34 D. Wang, H. Zhao, N. Q. Wu, M. A. E. Khakani and D. Ma, *J. Phys. Chem. Lett.*, 2010, **1**, 1030.
35 J. A. Seabold, K. Shankar, R. H. T. Wilke, M. Paulose, O. K. Varghese, C. A. Grimes and K.-S. Choi, *Chem. Mater.*, 2008, **20**, 5266.
36 M. Shang, W. Wang, L. Zhang, S. Sun, L. Wang and L. Zhou, *J. Phys. Chem. C*, 2009, **113**, 14727.
37 W. Zhou, H. Liu, J. Wang, D. Liu, G. Du and J. Cui, *ACS Appl. Mater. Interfaces*, 2010, **2**, 2385.
38 J. Lin, J. Shen, R. Wang, J. Cui, W. Zhou, P. Hu, D. Liu, H. Liu, J. Wang, R. I. Boughton and Y. Yue, *J. Mater. Chem.*, 2011, **21**, 5106.
39 W. Zhou, G. Du, P. Hu, G. Li, D. Wang, H. Liu, J. Wang, R. I. Boughton, D. Liu and H. Jiang, *J. Mater. Chem.*, 2011, **21**, 7937.
40 Y. Xu and M. A. A. Schoonen, *Am. Mineral.*, 2000, **85**, 543.
41 L. Li and B. Yan, *J. Non-Cryst. Solids*, 2009, **355**, 776.
42 S. Shamaila, A. K. L. Sajjad, F. Chen and J. Zhang, *Appl. Catal., B*, 2010, **94**, 272.
43 M. Gui, W. Zhang, Q. Su and C. Chen, *J. Solid State Chem.*, 2011, **184**, 1977.
44 H. Zhang, M. Lü, S. Liu, L. Wang, Z. Xiu, Y. Zhou, Z. Qiu, A. Zhang and Q. Ma, *Mater. Chem. Phys.*, 2009, **114**, 716.
45 W. F. Yao, X. H. Xu, H. Wang, J. T. Zhou, X. N. Yang, Y. Zhang, S. X. Shang and B. B. Huang, *Appl. Catal., B*, 2004, **52**, 109.
46 N. Mochida and J. Takahashi, *J. Ceram. Soc. Jpn.*, 1976, **84**, 413.
47 E. P. Meagher and G. A. Lager, *Can. Mineral.*, 1979, 77.
48 E. C. Subbarao, *Phys. Rev.*, 1961, **122**, 804.
49 A. H. Nethercot Jr, *Phys. Rev. Lett.*, 1974, **33**, 1088.
50 X. P. Lin, F. Q. Huang, W. D. Wang and K. L. Zhang, *Appl. Catal., A*, 2006, **307**, 257.
51 W. Wei, Y. Dai and B. Huang, *J. Phys. Chem. C*, 2009, **113**, 5658.